



Ground-based all-sky  
mid-infrared and  
visible imagery

D. I. Klebe et al.

This discussion paper is/has been under review for the journal Atmospheric Measurement Techniques (AMT). Please refer to the corresponding final paper in AMT if available.

# Ground-based all-sky mid-infrared and visible imagery for purposes of characterizing cloud properties

D. I. Klebe<sup>1,4</sup>, R. D. Blatherwick<sup>2,4</sup>, and V. R. Morris<sup>3</sup>

<sup>1</sup>Denver Museum of Nature and Science, Denver, Colorado, USA

<sup>2</sup>University of Denver, Denver, Colorado, USA

<sup>3</sup>Pacific Northwest National Laboratory, Richland, Washington, USA

<sup>4</sup>Solmirus Corporation, Woodland Park, Colorado, USA

Received: 31 May 2013 – Accepted: 13 August 2013 – Published: 29 August 2013

Correspondence to: D. I. Klebe (dimitri.klebe@dmns.org)

Published by Copernicus Publications on behalf of the European Geosciences Union.

Title Page

Abstract

Introduction

Conclusions

References

Tables

Figures



Back

Close

Full Screen / Esc

Printer-friendly Version

Interactive Discussion



## Abstract

This paper describes the All Sky Infrared Visible Analyzer (ASIVA), a multi-purpose visible and infrared sky imaging and analysis instrument whose primary function is to provide radiometrically calibrated imagery in the mid-infrared (mid-IR) atmospheric window. This functionality enables the determination of diurnal hemispherical cloud fraction (HCF) and estimates of sky/cloud temperature from which one can derive estimates of cloud emissivity and cloud height. This paper describes the calibration methods and performance of the ASIVA instrument with particular emphasis on data products being developed for the meteorological community. Data presented here were collected during a field campaign conducted at the Atmospheric Radiation Measurement (ARM) Southern Great Plains (SGP) Climate Research Facility from 21 May to 27 July 2009. The purpose of this campaign was to determine the efficacy of IR technology in providing reliable nighttime HCF data. Significant progress has been made in the analysis of the campaign data over the past several years and the ASIVA has proven to be an excellent instrument for determining HCF as well as several other important cloud properties.

## 1 Introduction

Uncertainty in the characterization of clouds in general circulation models (GCMs) is one of the major causes of the broad range of future climate change predictions (Atmospheric System Research (ASR) Science and Program Plan, January 2010). Hemispherical Cloud Fraction (HCF), which is closely related to cloud fraction (a dominant modulator of radiative fluxes), has been an integral part of the observational dataset that feed these GCMs (Kassianov et al., 2005). HCF, however, has only been directly determined at the ARM sites during daytime hours utilizing the Total Sky Imager (TSI) (Long et al., 2001). Other indirect cloud fraction data products can be derived from surface radiometers and the statistical analysis of lidar and radar observations (Qian

# AMTD

6, 7985–8019, 2013

## Ground-based all-sky mid-infrared and visible imagery

D. I. Klebe et al.

Title Page

Abstract

Introduction

Conclusions

References

Tables

Figures

◀

▶

◀

▶

Back

Close

Full Screen / Esc

Printer-friendly Version

Interactive Discussion



## Ground-based all-sky mid-infrared and visible imagery

D. I. Klebe et al.

Title Page

Abstract

Introduction

Conclusions

References

Tables

Figures

⏪

⏩

◀

▶

Back

Close

Full Screen / Esc

Printer-friendly Version

Interactive Discussion

et al., 2012). A direct means of determining nighttime HCF has been and remains a critical programmatic gap in ARM's observational dataset and is an important factor in understanding the life cycle of clouds, one of the central themes of the ASR program. The mid-infrared (mid-IR) atmospheric window from 8–13 microns ( $\mu\text{m}$ ) has long been known to hold great promise in closing this gap as well as providing other valuable ground-based cloud properties and atmospheric data (Shaw et al., 2005; Thurairajah and Shaw, 2005). A thermal IR imager has the distinct advantage of directly detecting emission from clouds, rather than relying on scattered light or obscured starlight, and is not hampered by the presence of the Sun or the Moon, thus providing consistent and reliable information under a wide variety of conditions. A major challenge for thermal imagers has been separating the effects of water vapor emission from that of cloud emission, particularly cirrus clouds (Brocard et al., 2011). The ASIVA's primary function is to provide radiometrically-calibrated imagery across the entire sky in the mid-IR. Figure 1 shows the clear-sky downwelling radiance as simulated using MODTRAN (Berk et al., 1999) for a standard mid-latitude summer atmosphere pointed at the zenith for 22 mm of precipitable water vapor (PWV), typical of conditions found at the ARM SGP site. Absorption and therefore thermal emission is dominated by water vapor at wavelengths less than 8  $\mu\text{m}$ , by carbon dioxide at wavelengths greater than 13  $\mu\text{m}$ , and by ozone near 9.5  $\mu\text{m}$ . Water vapor absorption lines are present throughout this spectral interval but are least prevalent in the 10.2–12.2  $\mu\text{m}$  region. For this reason, a custom 10.2–12.2  $\mu\text{m}$  filter for optimizing clear-sky/cloud contrast was fabricated for the ASIVA instrument. The spectral response of this filter (*shown in red*) as well the 8.25–9.25  $\mu\text{m}$  filter (*shown in blue*) used in this research are presented in Fig. 1.

This paper will discuss the ASIVA instrument with particular emphasis on the calibration procedures that have been developed to improve mid-IR radiometric performance enabling the removal of water vapor emission. Infrared data analysis procedures that are being developed to characterize cloud properties with particular emphasis on determining HCF will also be discussed. In addition, HCF data from ASIVA's visible channel







## 3.2 Calibration of spectral radiance images

The sky's spectral radiance ( $F_{\lambda_{\text{Sky}}}$ ) for a given filter is then determined using Eq. (3).

$$F_{\lambda_{\text{Sky}}} = \frac{I_{\lambda_{\text{Sky}}} - I_{\lambda_{\text{Ref}}}}{G_{\lambda}} + \text{BB}_{\lambda}(T_{\text{Ref}}) \left\{ \text{W m}^{-2} \mu\text{m}^{-1} \text{sr}^{-1} \right\}, \quad (3)$$

where  $I_{\lambda_{\text{Sky}}}$  = Instrumental Counts measured for the sky image,  $I_{\lambda_{\text{Ref}}}$  = Instrumental Counts measured for the reference blackbody image,  $G_{\lambda}$  = Instrument response coefficients derived from Eq. (1), and  $\text{BB}_{\lambda}(T_{\text{Ref}})$  = Integrated Blackbody Radiance derived from Eq. (2) for ambient temperature  $T_{\text{Ref}}$ .

A useful quantity utilized in the analysis presented in Sect. 4 is the normalized spectral radiance  $\mathcal{F}_{\lambda_{\text{Sky}}}$  given by Eq. (4). The normalized spectral radiance  $\mathcal{F}_{\lambda_{\text{Sky}}}$  can be thought of as a proxy to the sky's average emissivity.  $\mathcal{F}_{\lambda_{\text{Sky}}}$  is generally an underestimate of the true emissivity since the ambient temperature given by  $T_{\text{Ref}}$  is nominally greater than the mean temperature of the emitting sky.

$$\mathcal{F}_{\lambda_{\text{Sky}}} = F_{\lambda_{\text{Sky}}} / \text{BB}_{\lambda}(T_{\text{Ref}}) \quad (4)$$

## 4 Cloud detection and hemispherical cloud fraction analysis

### 4.1 Verification of calibration procedures

The calibration procedures described in Sect. 3 provide the foundation for cloud detection and other cloud data products that can be derived from the ASIVA instrument. As a verification of these procedures, ASIVA spectral radiance data were compared with the precisely calibrated data retrieved from the Atmospheric Emitted Radiance Interferometer (AERI) instrument available for the campaign period. The mean spectral radiance was determined by averaging the AERI spectral radiance data over the response of each of the two ASIVA IR channels as depicted in Fig. 5. The 8 min average

Title Page

Abstract

Introduction

Conclusions

References

Tables

Figures

◀

▶

◀

▶

Back

Close

Full Screen / Esc

Printer-friendly Version

Interactive Discussion



## Ground-based all-sky mid-infrared and visible imagery

D. I. Klebe et al.

Title Page

Abstract

Introduction

Conclusions

References

Tables

Figures

◀

▶

◀

▶

Back

Close

Full Screen / Esc

Printer-friendly Version

Interactive Discussion



AERI data were utilized, as this cadence was similar to the 5 min cadence used by the ASIVA instrument. Calibrated ASIVA data were then evaluated at the zenith, coincident with AERI's field-of-view. Comparison plots of AERI data with ASIVA data for the two daytime periods that will be highlighted in this paper are shown in Fig. 6. Agreement is very good ( $< 5\%$ ) for the two daytime comparisons and are representative of the entire campaign dataset. Note that the agreement is good in both clear and cloudy circumstances.

### 4.2 Removal of clear-sky emission

The primary step in the cloud detection process is to remove the effects of clear-sky emission. This is done by employing the all-sky capabilities of the ASIVA instrument. Figure 7 illustrates the procedure in which the clear-sky normalized radiance is determined from the ASIVA IR image dataset. In Fig. 7a, the normalized radiance pixel data are plotted as a function of airmass for the image shown in Fig. 7b. The normalized radiance data are sorted into 29 airmass bins of roughly equal pixel count. The lower envelope of points in each airmass bin (*shown as red squares*) is fit to a 2nd-order polynomial equation (*gold line*) which identifies the clear-sky radiance. Even in this very cloudy image the lower envelop is still well defined ( $\chi\text{-square} = 0.0002$ ) and serves as an excellent representation of the underlying clear-sky emission. The clear-sky emission is then described as a function of airmass utilizing this polynomial equation and is then subtracted from the original normalized radiance image to yield the clear-sky subtracted image shown in Fig. 7b. This image forms the basis of cloud fraction determination. A cloud/no cloud decision can be simply made by choosing a single threshold value, above which an individual pixel is determined to be cloudy. Two thresholds can be used to determine the presence of “thin” and “opaque” clouds, the criteria employed by the TSI instrument. The advantage of expressing the clear-sky subtracted image in normalized radiance is that as mentioned it is related to the emissivity of the cloud and is largely independent of ambient temperature.

## Ground-based all-sky mid-infrared and visible imagery

D. I. Klebe et al.

Title Page	
Abstract	Introduction
Conclusions	References
Tables	Figures
◀	▶
◀	▶
Back	Close
Full Screen / Esc	
Printer-friendly Version	
Interactive Discussion	

One of the primary challenges of producing a robust cloud decision map is determining the clear-sky radiance in nearly 100 % cloudy conditions. This is accomplished by demanding that the chi-square value for the polynomial fit be less than some threshold (chosen to be 0.002 in this analysis) to ensure a strict goodness-of-fit criterion. If this criterion is not met, the previous polynomial equation that has met this criterion is used to define the clear-sky radiance. We have found this procedure to be very effective. A case in which the sky is nearly 100 % cloudy is illustrated in Fig. 8. Note that the fit denotes the proper clear-sky radiance for this image.

### 4.3 Hemispherical cloud fraction determination

After determining the clear-sky emission, cloud decision masks can be processed by applying the proper thresholds to the clear-sky subtracted images. Using the thresholds (in normalized radiance units) of  $0.03 < \textit{thin cloud} < 0.05$  and  $\textit{opaque cloud} \geq 0.05$ , the HCF comparison plots derived for 21 July 2009 are shown in Fig. 9.

Agreement between TSI data retrieved from the ARM archive and the ASIVA IR data for this day is excellent. Note that the TSI instrument shows erroneous cloud fraction results at the beginning and end of the day. The low sun elevation angles prove more difficult for the TSI instrument. A more sophisticated analysis package is available (Long, 2010) to improve the TSI dataset and will be used for further comparison with ASIVA data.

21 July was dominated by thick opaque clouds. The 25 May 2009 dataset, which provided a mix of thin and opaque clouds, represents more challenging conditions for cloud fraction analysis. Figure 10 illustrates the difficulty in determining thin clouds. The problem arises in that the thin cirrus clouds evident in Fig. 10b (*deep blue color*) are below the thin cloud threshold of 0.03 used in the analysis of the 21 July 2009 dataset. As can be seen in Fig. 11 below, much better agreement (in particular for thin cloud determination) with TSI data can be achieved by lowering this threshold to 0.016. However applying this analysis to the 21 July dataset would produce a larger fraction of thin clouds than shown in Fig. 9. It may be that these thin clouds are indeed present



## Ground-based all-sky mid-infrared and visible imagery

D. I. Klebe et al.

Title Page	
Abstract	Introduction
Conclusions	References
Tables	Figures
◀	▶
◀	▶
Back	Close
Full Screen / Esc	
Printer-friendly Version	
Interactive Discussion	

but that the TSI is insensitive to thin clouds in highly overcast conditions. Presently we are adopting a variable lower thin cloud threshold that is dependent on opaque cloud fraction to achieve better agreement with TSI data in both of these circumstances. Basically the thin cloud threshold will be lowered in clearer sky conditions. Ultimately, we do not expect perfect agreement as the cloud decision analysis is fundamentally different between the IR and visible. However, the primary goal of this research has been to obtain as close agreement as possible between the TSI and ASIVA instrument.

### 4.4 Retrieval of HCF data product from ASIVA visible data

Retrieval of the HCF data product from ASIVA's visible channels uses the same analysis adopted by the TSI instrument. The first-order analysis involves taking the ratio of the red image to blue image and then setting appropriate opaque/thin/no cloud thresholds (Long et al., 2006). Second-order analysis requires taking into account the Sun's position in the sky and adopting a varying threshold depending on a pixel's relative position to the Sun. Second-order analysis is easily implemented in the ASIVA instrument but was not used in the analysis presented below as it was not used in the dataset retrieved from the ARM archive. Figure 12 shows the visible red/blue ratio images coincident with the IR images shown in Figs. 7 and 10. Note that the images in Fig. 12 are at 90° relative to those in Figs. 7 and 10. The sun has been occulted in software (the larger circle) and is similar in size to the zone-of-avoidance utilized in the TSI cloud fraction analysis. In addition, a small circle is used to mask an artifact seen at the sun's position reflected through the zenith. This artifact (which can be seen in Fig. 3) is brought about by internal reflection within the fisheye lens. Since the ASIVA instrument does not require a sun occulter like that utilized in the TSI instrument, eliminating this part of sky is relatively minor in the analysis.

Thresholds are then set to define the thin and opaque boundaries to provide the best agreement with the TSI instrument. Figure 13 shows the cloud fraction analysis for 21 July 2009. In contrast to the TSI, the ASIVA visible channel performs very well





filters but is insensitive to the total optical depth. For this reason we believe that color temperature will ultimately yield a better measure of the true temperature for optically thin clouds. Color temperature images are shown in Fig. 16.

Both of the images in Fig. 16 show variations (both positive and negative temperature fluctuations) at the periphery of the clouds due to the motion of the clouds over the data acquisition period. This is particularly evident in the 21 July image as the clouds were very fast moving. Current ASIVA instruments now acquire 8.25–9.25  $\mu\text{m}$  and 10.2–12.2  $\mu\text{m}$  image data in a much shorter time interval to combat this problem. Also note that the clear-sky color temperature is higher (one would expect lower temperatures) at the zenith due to sky emissivity differences in the two IR filters. Color temperatures in the optically thick regions of clouds shown in Fig. 16 are consistent with those of Fig. 15 and both indicate cloud temperatures 10–20 K below the ground temperature. To some degree, these color maps already provide an estimate of cloud temperature that may be very valuable to cloud modelers. To improve on the accuracy of this measurement, one will have to account for the intervening atmospheric absorption and emission in each of the filters. This is where knowledge of PWV (discussed in Sect. 5.3) is required to provide additional information regarding the atmosphere’s radiative properties.

## 5.2 Determination of sky/cloud emissivity

Perhaps one of the most powerful data products that can be derived using the temperature analysis outlined above is an accurate estimate of the emissivity of an image. By assuming that the color temperature is indeed a measure of the true mean temperature for an image, one can compute a blackbody radiance image from the color temperature image. By dividing the measured radiance by the blackbody radiance derived from the color temperature, one arrives at a measure of the emissivity of the sky. Figure 17 shows the results of this analysis.

The accuracy of this measure is somewhat hampered by the variations in emissivity between the two IR filters but can be corrected using knowledge of the PWV burden and the information it yields regarding the atmosphere’s radiative properties. Ignoring

## Ground-based all-sky mid-infrared and visible imagery

D. I. Klebe et al.

Title Page

Abstract

Introduction

Conclusions

References

Tables

Figures



Back

Close

Full Screen / Esc

Printer-friendly Version

Interactive Discussion



the effects of cloud motion the images of Fig. 17 show cloud emissivity near unity for opaque clouds as one would expect. They also show the expected variations in clear-sky emissivity (i.e. lower emissivity at the zenith and higher emissivity near the horizon).

### 5.3 Determination of precipitable water vapor (PWV)

As discussed above, determination of PWV is important as it can provide valuable ancillary information in the analysis of other cloud property data products, in particular refining cloud temperature measurements. The basic analysis strategy is to compare the clear-sky envelope (described in Sect. 4.2) with modeled data. The model data are constructed using a series of MODTRAN simulations that provide a parameterization of the normalized clear-sky downwelling radiance as a function of PWV evaluated at different elevation angles (i.e. airmass). Preliminary simulations have been run for each of ASIVA's filters using a standard mid-latitude summer atmosphere at sea level and a lapse rate extracted from a radiosonde dataset acquired for 21 July 2009. The simulated dataset is then best fit to the clear-sky envelope determined for a particular image thus providing an estimate of PWV. Figure 18 shows the result of this analysis for the 25 May 2009 and 21 July 2009 datasets. The PWV data are compared with that retrieved from the Microwave Radiometer (MWR), an instrument with accuracy of better than 1 mm PWV. The correlation is fairly good for the 21 July dataset (the day from which the radiosonde data was used in the MODTRAN analysis) but deviates significantly for the 25 May dataset. This suggests coincidental radiosonde data may be required to improve the accuracy of ASIVA's estimate of PWV.

Better accuracy in the determination of PWV may not be required in that this measure is only required to make second order corrections to data products such as the sky/cloud temperature images. If better accuracy is required, other instruments such as MWR could be used in a value added product (VAP).

## Ground-based all-sky mid-infrared and visible imagery

D. I. Klebe et al.

Title Page

Abstract

Introduction

Conclusions

References

Tables

Figures



Back

Close

Full Screen / Esc

Printer-friendly Version

Interactive Discussion



## 5.4 Determination of cloud height

Cloud height can be estimated from ASIVA cloud temperature images by utilizing the altitude vs. temperature information retrieved from radiosonde data. Figure 19 shows the comparison of cloud height derived from ASIVA brightness temperature images at zenith with cloud height measurements retrieved from the ARM ceilometer (CEIL) operated at SGP during the campaign period. Only very opaque clouds (*opaque cloud*  $\geq 0.3$ ) were used in deriving cloud height measurements in these comparisons to insure that the clouds were optically thick and that their brightness temperature was a good estimate of the cloud temperature. Agreement is good for the 25 May dataset but varies significantly for the low clouds seen in the 21 July dataset. This is presumably due to the clouds being much cooler than where the lapse rate would place them. In addition, the ASIVA instrument measures the mean temperature of the cloud to one optical depth. This will always be located at a higher altitude than the cloud base.

## 6 Conclusions

The ASIVA demonstrates considerable promise in providing a diurnal hemispherical cloud fraction data product. ASIVA HCF data (both IR and Visible) correlate very well with daytime data retrieved from the Total Sky Imager. Radiometric calibration procedures have been validated by data retrieved from the Atmospheric Emitted Radiance Interferometer. The quality of the ASIVA's radiometric data promises to yield additional products such as quality estimates of cloud temperature (both color and brightness temperature), sky/cloud emissivity, precipitable water vapor, and cloud height.

AMTD

6, 7985–8019, 2013

### Ground-based all-sky mid-infrared and visible imagery

D. I. Klebe et al.

Title Page

Abstract

Introduction

Conclusions

References

Tables

Figures

⏪

⏩

◀

▶

Back

Close

Full Screen / Esc

Printer-friendly Version

Interactive Discussion



*Acknowledgements.* This research was supported in part by the US Department of Energy's (DOE) Atmospheric System Research Program, an Office of Science, Office of Biological and Environmental Research program, under Grant DE-SC-0008650. We acknowledge the cooperation of the DOE Atmospheric Radiation Measurement Climate Research Facility Southern Great Plains site and thank those responsible for the operation and maintenance of the instruments that produced the data used in this study.

## References

- Berk, A., Anderson, G. P., Bernstein, L. S., Acharya, P. K., Dothe, H., Matthew, M. W., Adler-Golden, S. M., Chetwynd, J. H., Richtmeier, S. C., Pukall, B., Alfred, C. L., Jeong, L. S., and Hoke, M. L.: Modtran4 radiative transfer modeling for atmospheric correction, *P. Soc. Photo-Opt. Ins.*, 3756, 348–353, 1999.
- Brocard, E., Schneebeli, M., and Mätzler, C.: Detection of cirrus clouds using infrared radiometry, *IEEE T. Geosci. Remote*, 49, 595–602, 2011.
- Kassianov, E., Long, C. N., and Ovtchinnikov, M.: Cloud sky cover vs. cloud fraction: whole-sky simulations and observations, *J. Appl. Meteorol.*, 44, 86–98, 2005.
- Klebe, D., Sebag, J., Blatherwick, R. D., and Zimmer, P. C.: All-sky mid-infrared imagery to characterize sky conditions and improve astronomical observational performance, *Publ. Astron. Soc. Pac.*, 124, 1309–1317, 2012.
- Long, C. N.: Correcting for circumsolar and near-horizon errors in sky cover retrievals from sky images, *Open Atmos. Sci. J.*, 4, 45–52, 2010.
- Long, C. N., Slater, D. W., and Tooman, T.: Total Sky Imager (TSI) Model 880 Status and Testing Results, Atmospheric Radiation Measurement Program Technical Report, ARM TR-004, 2001.
- Long, C. N., Sabburg, J. M., Calbó, J., PagLong, C. N., Sabburg, J. M., Calbó, J., and Pages, D.: Retrieving cloud characteristics from ground-based daytime color all-sky images, *J. Atmos. Ocean. Tech.*, 23, 633–652, 2006.
- Shaw, J. A., Nugent, P. W., Pust, N. J., Thurairajah, B., and Mizutani, K.: Radiometric cloud imaging with an uncooled microbolometer thermal infrared camera, *Opt. Express*, 13, 5807–5817, 2005.

## Ground-based all-sky mid-infrared and visible imagery

D. I. Klebe et al.

Title Page

Abstract

Introduction

Conclusions

References

Tables

Figures

◀

▶

◀

▶

Back

Close

Full Screen / Esc

Printer-friendly Version

Interactive Discussion



Thurairajah, B. and Shaw, J. A.: Cloud statistics measured with the infrared cloud imager (ICI), IEEE T. Geosci. Remote, 43, 2000–2007, 2005.

5 Qian, Y., Long, C. N., Wang, H., Comstock, J. M., McFarlane, S. A., and Xie, S.: Evaluation of cloud fraction and its radiative effect simulated by IPCC AR4 global models against ARM surface observations, Atmos. Chem. Phys., 12, 1785–1810, doi:10.5194/acp-12-1785-2012, 2012.

## AMTD

6, 7985–8019, 2013

### Ground-based all-sky mid-infrared and visible imagery

D. I. Klebe et al.

Title Page

Abstract

Introduction

Conclusions

References

Tables

Figures



Back

Close

Full Screen / Esc

Printer-friendly Version

Interactive Discussion



**Ground-based all-sky  
mid-infrared and  
visible imagery**

D. I. Klebe et al.

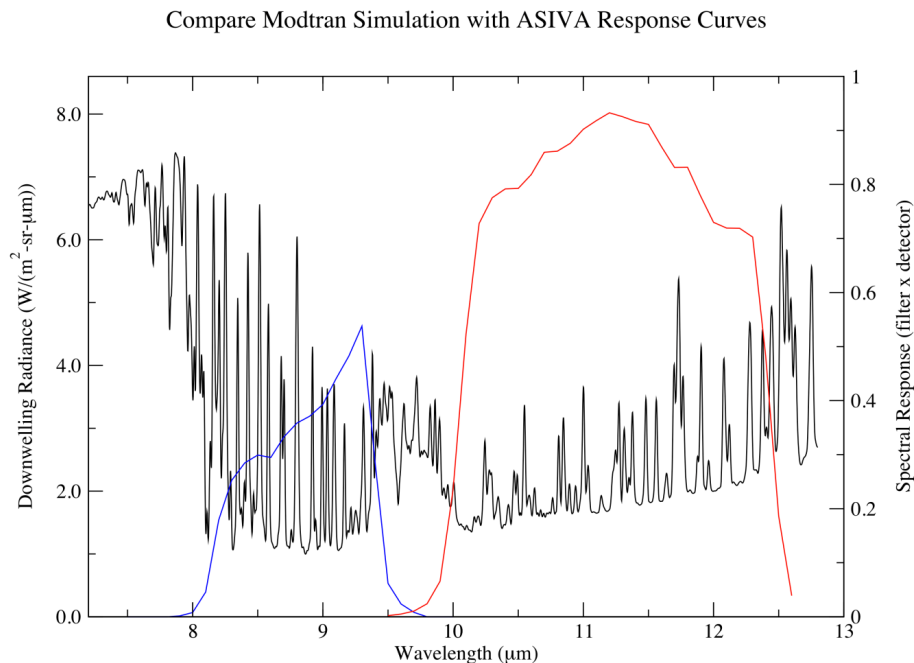


**Fig. 1.** Simulated clear-sky downwelling radiance for 22 mm PWV pointed at the zenith. Spectral response of two ASIVA filters (red and blue) used in this research.

Title Page

Abstract

Introduction

Conclusions

References

Tables

Figures

◀

▶

◀

▶

Back

Close

Full Screen / Esc

Printer-friendly Version

Interactive Discussion





**Fig. 2.** ASIVA at SGP Guest Instrument Facility from 21 May to 27 July 2009.

# AMTD

6, 7985–8019, 2013

## Ground-based all-sky mid-infrared and visible imagery

D. I. Klebe et al.

Title Page

Abstract

Introduction

Conclusions

References

Tables

Figures

⏪

⏩

◀

▶

Back

Close

Full Screen / Esc

Printer-friendly Version

Interactive Discussion



# AMTD

6, 7985–8019, 2013

## Ground-based all-sky mid-infrared and visible imagery

D. I. Klebe et al.

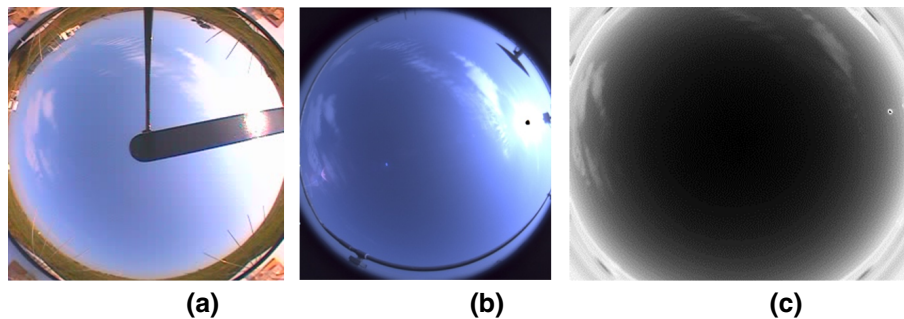


**Fig. 3.** Three all-sky images acquired on 3 July 2009 at 13:32 UTC. **(a)** TSI, **(b)** ASIVA Visible, and **(c)** ASIVA IR 10.2–12.2 μm.

Title Page

Abstract

Introduction

Conclusions

References

Tables

Figures

◀

▶

◀

▶

Back

Close

Full Screen / Esc

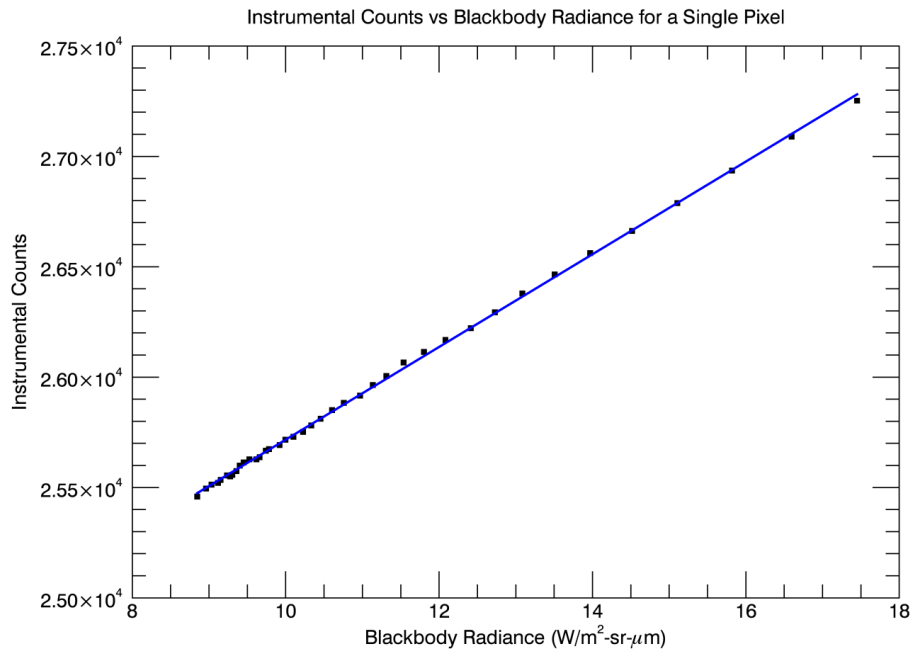
Printer-friendly Version

Interactive Discussion



**Ground-based all-sky  
mid-infrared and  
visible imagery**

D. I. Klebe et al.

**Fig. 4.** 10.2–12.2  $\mu\text{m}$  instrument response for a single central pixel.

Title Page

Abstract

Introduction

Conclusions

References

Tables

Figures

◀

▶

◀

▶

Back

Close

Full Screen / Esc

Printer-friendly Version

Interactive Discussion



**Ground-based all-sky  
mid-infrared and  
visible imagery**

D. I. Klebe et al.

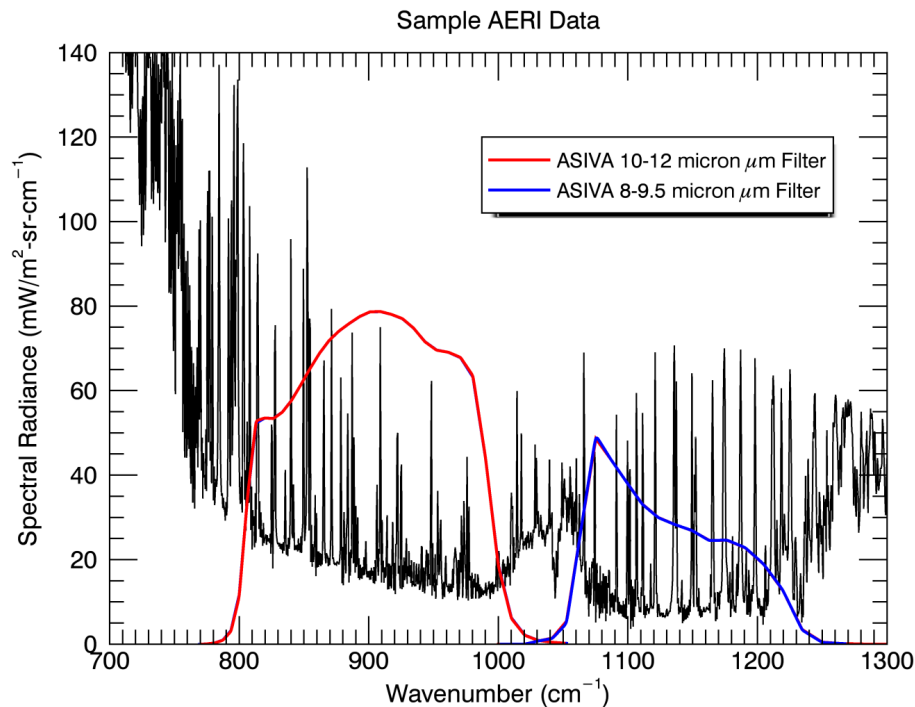


**Fig. 5.** Sample AERI data indicating ASIVA's 10.2–12.2  $\mu\text{m}$  (red line) and 8.25–9.25  $\mu\text{m}$  (blue line) instrument response for which the AERI spectral radiance data were averaged.

[Title Page](#)[Abstract](#)[Introduction](#)[Conclusions](#)[References](#)[Tables](#)[Figures](#)[◀](#)[▶](#)[◀](#)[▶](#)[Back](#)[Close](#)[Full Screen / Esc](#)[Printer-friendly Version](#)[Interactive Discussion](#)

## Ground-based all-sky mid-infrared and visible imagery

D. I. Klebe et al.

Title Page

Abstract

Introduction

Conclusions

References

Tables

Figures

⏪

⏩

◀

▶

Back

Close

Full Screen / Esc

Printer-friendly Version

Interactive Discussion

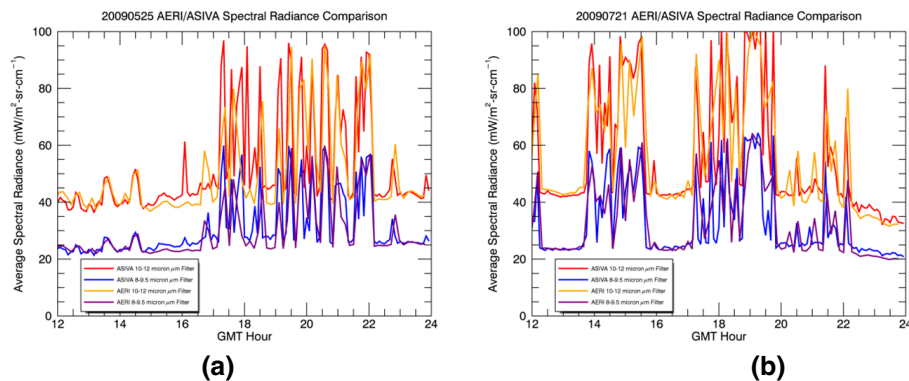


**Fig. 6.** Comparison of AERI with ASIVA spectral radiance data in each of the two filters for (a) 25 May 2009 and (b) 21 July 2009.

## Ground-based all-sky mid-infrared and visible imagery

D. I. Klebe et al.

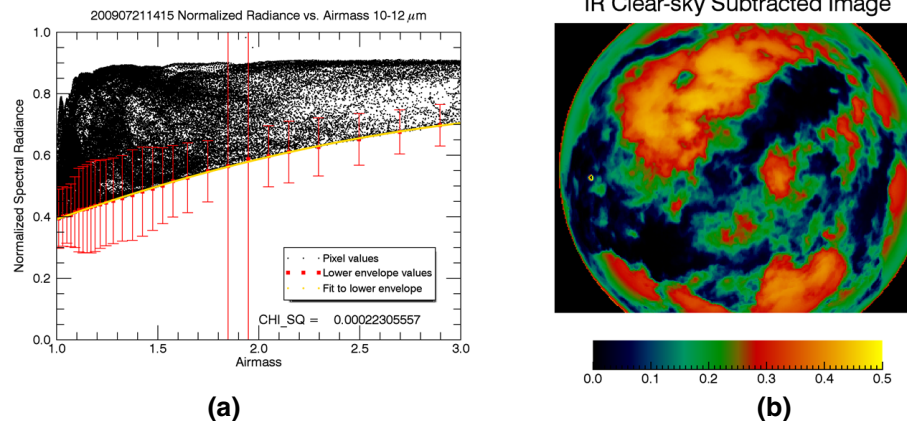


**Fig. 7.** (a) Pixel normalized radiance vs. airmass data. Gold line represents 2nd-order polynomial fit to lower envelope of points (red squares) in each of 29 airmass bins. (b) Clear-sky subtracted image based on analysis shown in (a). Note: image is truncated at six airmasses. Large error bars for airmass bins near 1.9 airmass are due to the sun's extreme pixel values.

Full Screen / Esc

Printer-friendly Version

Interactive Discussion



Ground-based all-sky  
mid-infrared and  
visible imagery

D. I. Klebe et al.

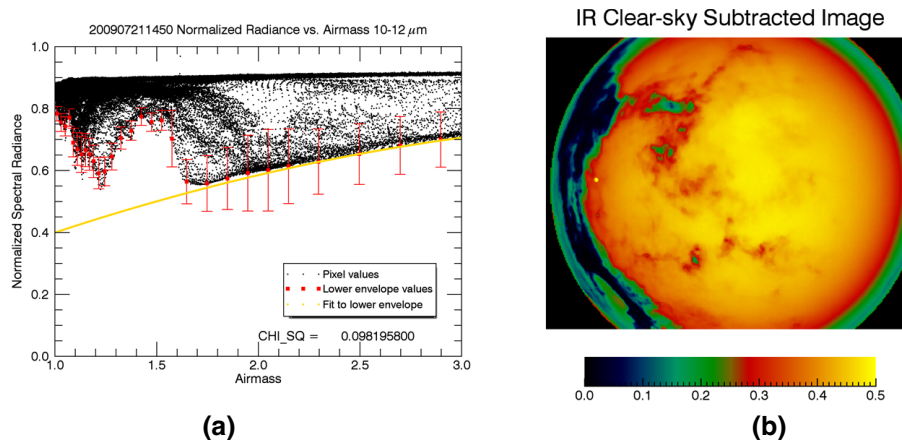


**Fig. 8.** (a) Pixel normalized radiance vs. airmass data. Gold line represents 2nd-order polynomial fit to lower envelope of points obtained from the previous dataset that met the chi-square  $< 0.002$  criterion. (b) Clear-sky subtracted image based on analysis shown in (a).

[Title Page](#)[Abstract](#)[Introduction](#)[Conclusions](#)[References](#)[Tables](#)[Figures](#)[◀](#)[▶](#)[◀](#)[▶](#)[Back](#)[Close](#)[Full Screen / Esc](#)[Printer-friendly Version](#)[Interactive Discussion](#)

**Ground-based all-sky  
mid-infrared and  
visible imagery**

D. I. Klebe et al.

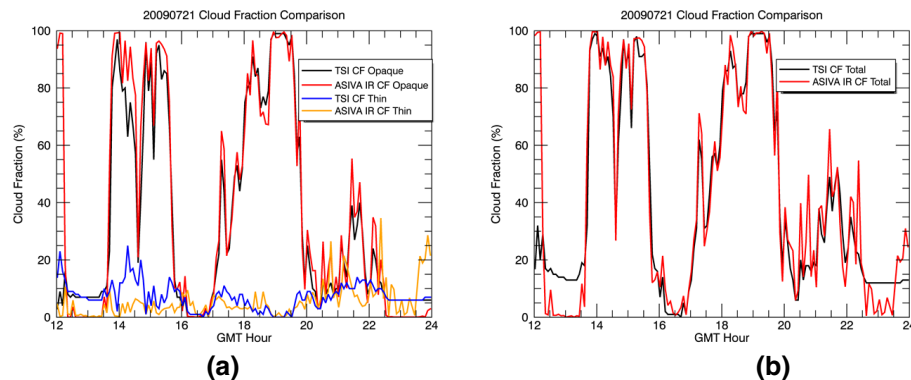


**Fig. 9.** (a) Hemispherical Cloud Fraction comparison between TSI and ASIVA IR for opaque and thin cloud types during daylight hours on 21 July 2009. (b) HCF comparison between TSI and ASIVA IR for total (opaque + thin) cloud fraction.

[Title Page](#)[Abstract](#)[Introduction](#)[Conclusions](#)[References](#)[Tables](#)[Figures](#)[⏪](#)[⏩](#)[◀](#)[▶](#)[Back](#)[Close](#)[Full Screen / Esc](#)[Printer-friendly Version](#)[Interactive Discussion](#)

**Ground-based all-sky mid-infrared and visible imagery**

D. I. Klebe et al.

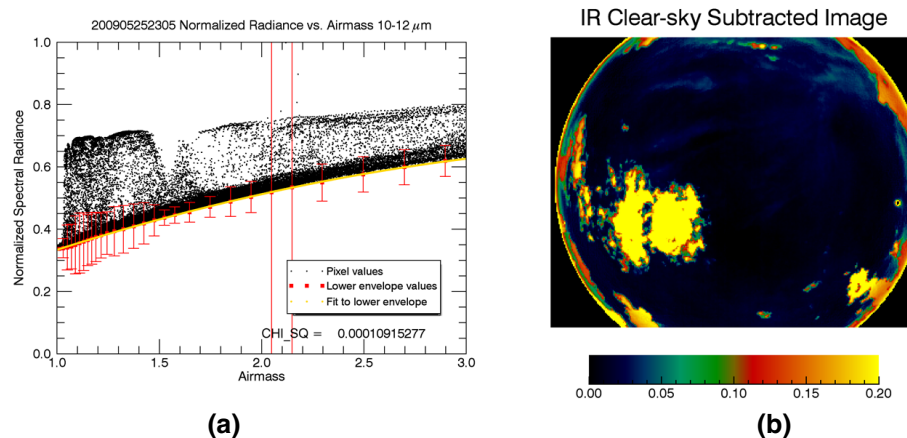


**Fig. 10.** (a) Pixel normalized radiance vs. airmass data. Gold line represents 2nd-order polynomial fit to lower envelope of points. (b) Clear-sky subtracted image based on analysis shown in (a).

Full Screen / Esc

Printer-friendly Version

Interactive Discussion



## Ground-based all-sky mid-infrared and visible imagery

D. I. Klebe et al.

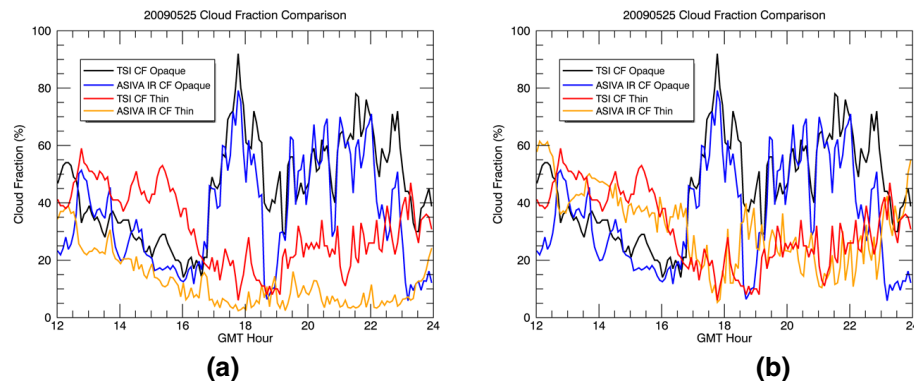


**Fig. 11.** (a) Cloud fraction comparison between TSI and ASIVA IR for thresholds  $0.03 < \text{thin cloud} < 0.05$  and  $\text{opaque cloud} \geq 0.05$  and (b)  $0.016 < \text{thin cloud} < 0.05$  and  $\text{opaque cloud} \geq 0.05$ .

Title Page

Abstract

Introduction

Conclusions

References

Tables

Figures

◀

▶

◀

▶

Back

Close

Full Screen / Esc

Printer-friendly Version

Interactive Discussion



**Ground-based all-sky  
mid-infrared and  
visible imagery**

D. I. Klebe et al.

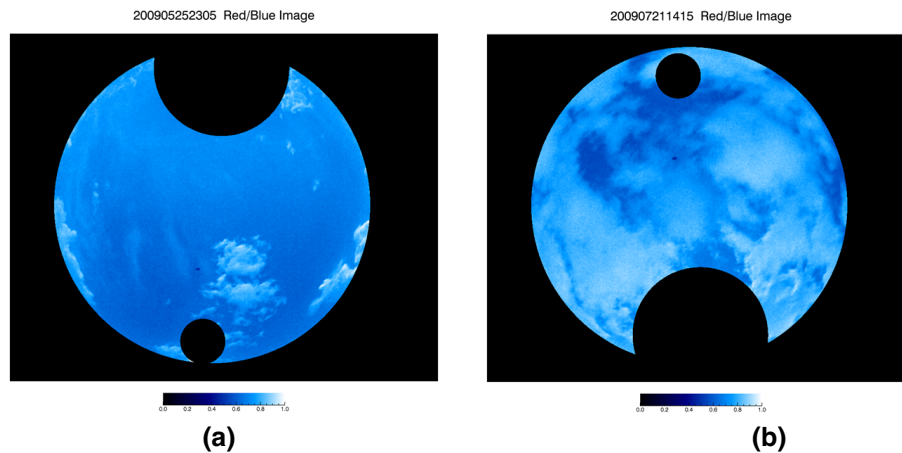


**Fig. 12.** (a) Red/Blue ratio image for 25 May 2009. (b) Red/Blue ratio image for 21 July 2009.

Title Page

Abstract

Introduction

Conclusions

References

Tables

Figures

◀

▶

◀

▶

Back

Close

Full Screen / Esc

Printer-friendly Version

Interactive Discussion



**Ground-based all-sky  
mid-infrared and  
visible imagery**

D. I. Klebe et al.

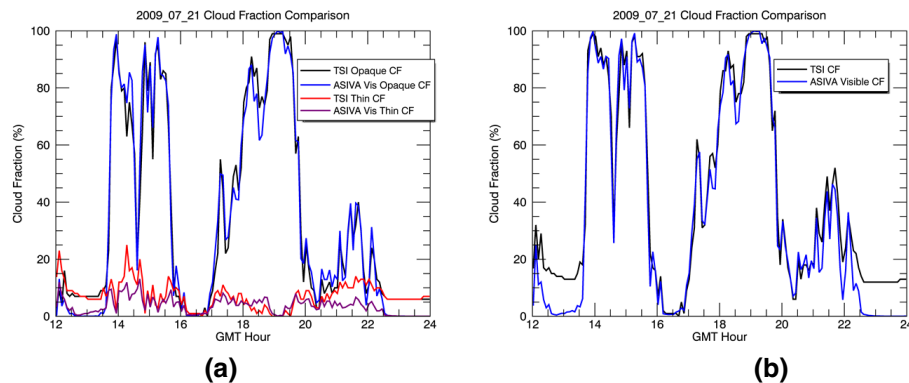


**Fig. 13.** (a) HCF comparison between TSI and ASIVA Visible for opaque and thin cloud types for 21 July 2009. (b) HCF comparison between TSI and ASIVA Visible for total (opaque + thin) cloud fraction.

[Title Page](#)[Abstract](#)[Introduction](#)[Conclusions](#)[References](#)[Tables](#)[Figures](#)[⏪](#)[⏩](#)[◀](#)[▶](#)[Back](#)[Close](#)[Full Screen / Esc](#)[Printer-friendly Version](#)[Interactive Discussion](#)

## Ground-based all-sky mid-infrared and visible imagery

D. I. Klebe et al.

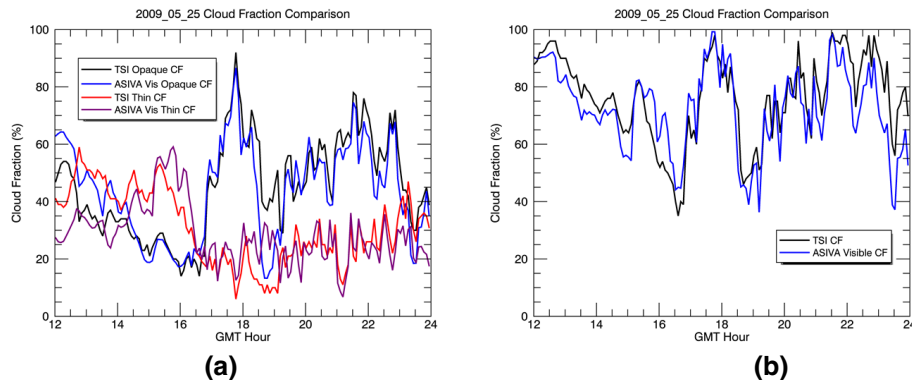


**Fig. 14.** (a) Cloud fraction comparison between TSI and ASIVA Visible for opaque and thin cloud types for 25 May 2009. (b) Cloud fraction comparison between TSI and ASIVA Visible for total (opaque + thin) cloud fraction.

Title Page

Abstract

Introduction

Conclusions

References

Tables

Figures

⏪

⏩

◀

▶

Back

Close

Full Screen / Esc

Printer-friendly Version

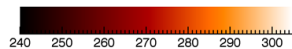
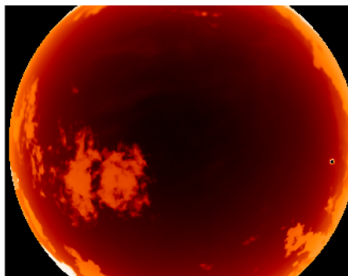
Interactive Discussion



**Ground-based all-sky  
mid-infrared and  
visible imagery**

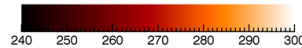
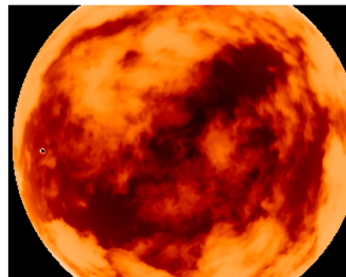
D. I. Klebe et al.

200905252305 Brightness Temperature



(a)

200907211415 Brightness Temperature



(b)

**Fig. 15.** Brightness temperature (K) for representative images on **(a)** 25 May 2009 and **(b)** 21 July 2009.

Title Page

Abstract

Introduction

Conclusions

References

Tables

Figures

◀

▶

◀

▶

Back

Close

Full Screen / Esc

Printer-friendly Version

Interactive Discussion



**Ground-based all-sky  
mid-infrared and  
visible imagery**

D. I. Klebe et al.

Title Page

Abstract

Introduction

Conclusions

References

Tables

Figures

◀

▶

◀

▶

Back

Close

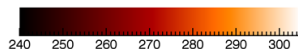
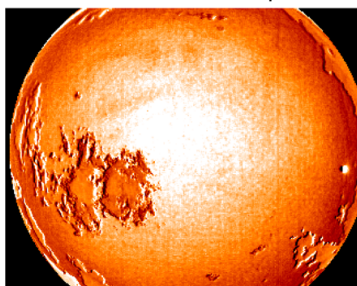
Full Screen / Esc

Printer-friendly Version

Interactive Discussion

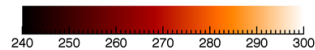
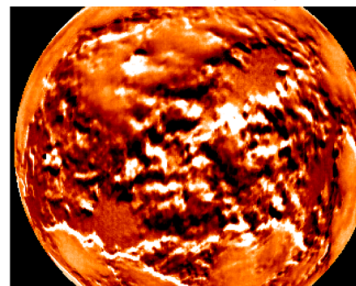


200905252305 Color Temperature



(a)

200907211415 Color Temperature



(b)

**Fig. 16.** Color temperature (K) for representative images on **(a)** 25 May 2009 and **(b)** 21 July 2009.

**Ground-based all-sky mid-infrared and visible imagery**

D. I. Klebe et al.

Title Page

Abstract

Introduction

Conclusions

References

Tables

Figures

◀

▶

◀

▶

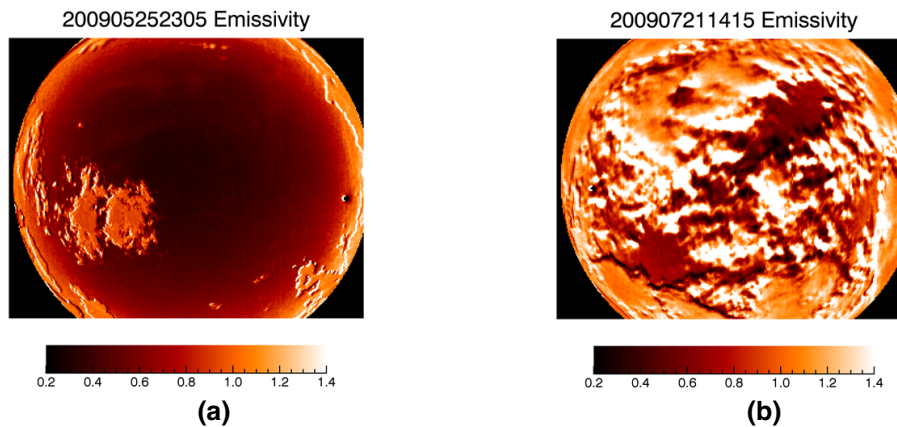
Back

Close

Full Screen / Esc

Printer-friendly Version

Interactive Discussion

**Fig. 17.** Emissivity for representative images on **(a)** 25 May 2009 and **(b)** 21 July 2009.

**Ground-based all-sky  
mid-infrared and  
visible imagery**

D. I. Klebe et al.

Title Page

Abstract

Introduction

Conclusions

References

Tables

Figures

◀

▶

◀

▶

Back

Close

Full Screen / Esc

Printer-friendly Version

Interactive Discussion

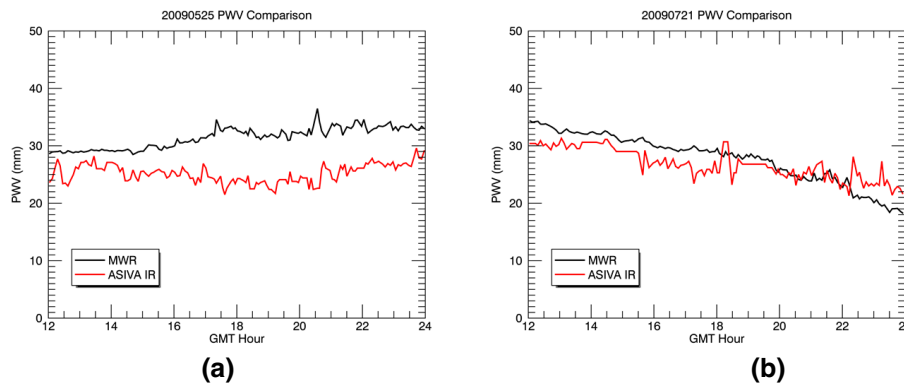


**Fig. 18.** Comparison of MWR with ASIVA PWV data for **(a)** 25 May 2009 and **(b)** 21 July 2009.

## Ground-based all-sky mid-infrared and visible imagery

D. I. Klebe et al.

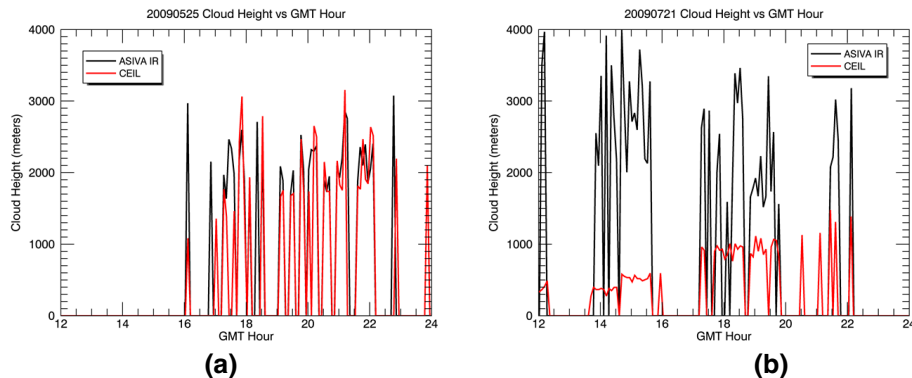


**Fig. 19.** Comparison of cloud height derived from ASIVA brightness temperature data with ceilometer data for **(a)** 25 May 2009 and **(b)** 21 July 2009.

[Title Page](#)[Abstract](#)[Introduction](#)[Conclusions](#)[References](#)[Tables](#)[Figures](#)[⏪](#)[⏩](#)[◀](#)[▶](#)[Back](#)[Close](#)[Full Screen / Esc](#)[Printer-friendly Version](#)[Interactive Discussion](#)